Coherent Structures Modulate Atmospheric Surface Layer Flux-Gradient Relationships

S. T. Salesky*
School of Meteorology, The University of Oklahoma, Norman, Oklahoma 73072, USA

W. Anderson
Mechanical Engineering Department, The University of Texas at Dallas, Richardson, Texas 75080, USA

(Received 31 January 2020; revised 6 March 2020; accepted 24 August 2020; published 16 September 2020)

Since its inception in the 1940s, Monin-Obukhov similarity theory (MOST), which relates turbulent fluxes to mean vertical gradients in the lower atmosphere, has become ubiquitous for predicting surface fluxes of quantities transported by the flow in numerical weather, climate, and hydrological forecasting models. Despite its widespread use, MOST does not account for the effects of large coherent structures in the flow, which modulate the amplitude of turbulent fluctuations, and are responsible for a large fraction of the total transport. Herein, we demonstrate that the incorporation of the large-scale streamwise velocity $u_l(\boldsymbol{x},t) = G_\delta \star u(\boldsymbol{x},t)$, where G_δ is a low-pass filtering kernel, into dimensional analysis leads to an additional dimensionless parameter $\alpha(\boldsymbol{x},t)$, which captures the modulating influence of these structures on flux-gradient relationships. Atmospheric observations and large-eddy simulations are used to demonstrate that observed deviations from MOST can indeed be explained by this new parameter; coherent structures induce an alternating loading and unloading of the mean velocity gradient near the surface.

DOI: 10.1103/PhysRevLett.125.124501

Introduction.—For over seven decades, Monin-Obukhov similarity theory (MOST), which relates turbulent fluxes to mean vertical gradients, has served as a unifying theory for studies of the atmospheric surface layer (ASL) [1,2]. In MOST, which extends the logarithmic law of the wall for wall-bounded turbulent shear flows [3] to flows with thermal stratification, one assumes that four governing scales are relevant for turbulence statistics in the ASL: wall-normal distance z, buoyancy parameter g/Θ_0 (where g is gravity and Θ_0 is a reference potential temperature), kinematic surface shear stress $-\tau_0/\rho = u_\tau^2 = -\overline{u'w'}$, and kinematic surface temperature flux $H_0/\rho c_p = \overline{w'\theta'}$. Dimensional analysis dictates $\Pi_1 = \phi(\Pi_2)$, where Π_1 is the dependent variable of interest (e.g., vertical gradient, variance, or spectral density) normalized by the MO scales, and $\Pi_2 = \zeta = z/L$ is the Monin-Obukhov stability variable, where $L = -u_\tau^3\Theta_0/\kappa g\overline{w'\theta'}$ is the Obukhov length and κ is the von Kármán constant. MO similarity predicts

$$\frac{\kappa z}{u_\tau}\frac{dU(z)}{dz} = \phi_m(\zeta) \tag{1}$$

for the dimensionless mean velocity gradient where $U(z) = \langle u(\boldsymbol{x},t)\rangle$ is the ensemble-mean streamwise velocity for a horizontally homogeneous ASL. The form of the MOST functions is not predicted by dimensional analysis; thus $\phi_m(\zeta)$ must be determined empirically.

Despite its widespread use [4,5], deviations from MOST have been widely documented by many investigators [6–10], undermining the prognostic capabilities of MOST for turbulent flux closure. Notably, Salesky *et al.* [9] demonstrated that deviations of calculated values of $\phi_m(\zeta)$ from MOST empirical curves could not be explained by so-called random errors, i.e., insufficient convergence of the time average to the true ensemble mean [11], indicating that additional physical processes are responsible for MOST deviations. Correct selection of additional governing scales in the dimensional analysis that account for these processes would lead to additional independent dimensionless groups, i.e., $\Pi_1 = \phi_m(\Pi_2, \Pi_3, \ldots, \Pi_n)$, which would, by definition, eliminate these deviations from MOST and enable collapse of calculated values of ϕ_m to a set of universal curves.

The originators of MOST selected the distance from the ground, z, as the normalizing lengthscale; this choice was presumably informed by contemporaneous insights from A. A. Townsend [12], who established the attached eddy hypothesis, where the wall itself regulates the spatial extent of turbulence. However, laboratory experiments and numerical simulations over the last several decades at high Reynolds numbers have revealed the existence of so-called large-scale motions (LSMs) [13–18], and very-large-scale motions (VLSMs) [19–23], coherent regions of high- and low-momentum fluid that respectively extend $\mathcal{O}(\delta)$ and

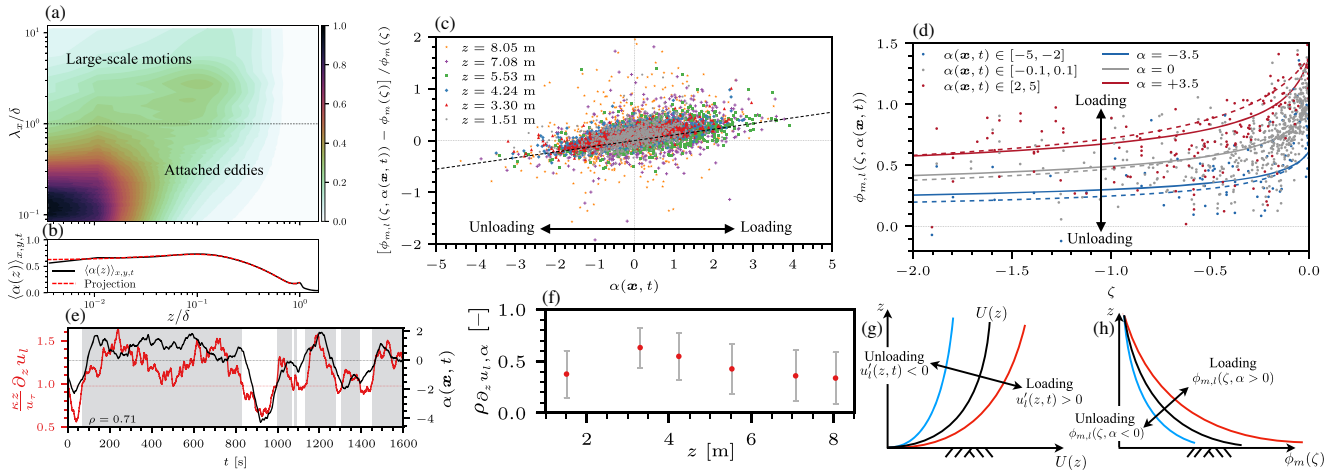

FIG. 1. Statistics from LES of the neutrally stratified ABL and AHATS data [9,47]. (a) Premultiplied spectrogram of streamwise velocity, $\pi\lambda_x^{-1}u_\tau^{-2}E_{\langle u'(\boldsymbol{x},t)^2\rangle_t}(\lambda_x,z)$, plotted versus dimensionless wall-normal distance (z/δ) and streamwise wavelength (λ_x/δ); (b) vertical profile of the similarity parameter $\langle\alpha(z)\rangle_{xyt}$, recovered from integrating the low-wave-number range of the spectrum [Eq. (11)]. (c),(d) Time-variable nondimensional velocity gradient attributes. Abscissa and ordinate in (c) are $\alpha(\boldsymbol{x},t)$ [Eq. (2)] and nondimensional velocity gradient variability, respectively [Eq. (4)]; data points shown based on AHATS tower measurement heights denoted on legend, while linear fit represents the right-hand side of Eq. (4). (d) Results of generalized empirical curves [solid curves; Eq. (6)], generalized O'KEYPS model [dashed curves; Eq. (7)], and data points from AHATS. (e) Time series of large-scale velocity gradient (red) and nondimensional parameter, $\alpha(\boldsymbol{x},t)$ (black) from AHATS data; gray panels denote elevated gradient due to $\alpha(\boldsymbol{x},t)>0$, where the correlation coefficient is $\rho=0.71$. (f) Vertical profile of large-scale gradient and $\alpha(\boldsymbol{x},t)$ correlation from the AHATS data; red markers denote mean value and gray bands denote standard deviation. (g),(h) Idealized large-scale velocity and velocity gradient with respect to ensemble-mean value, respectively, where the influence of unloading and loading is shown.

$\mathcal{O}(10\delta)$ in streamwise extent (where δ is the boundary layer depth). LSMs scale in extent with z, but undergo a streamwise coalescence to form VLSMs [22]. In addition to being responsible for a large fraction of the momentum and kinetic energy transport [20,21,24,25], LSMs, and VLSMs also modulate the amplitude (AM) and frequency (FM) of small-scale turbulent fluxes [26–31]; this modulation also occurs in thermally stratified flows, such as the ASL [31]. However, a similarity framework that captures the influence of LSMs on flux-gradient relationships has not been developed to date. We focus on unstable ($\zeta<0$) and neutral ($\zeta=0$) stratification in this Letter, given the importance of the convective atmospheric boundary layer (ABL) for evapotranspiration, convective initiation, etc.

Modulated near-wall gradient.—In order to capture the modulating influence of LSMs and VLSMs on flux-gradient relationships, we revisit the dimensional analysis of Monin and Obukhov, but incorporate a velocity scale that captures the influence of large coherent structures present in the flow. Specifically, we include the large-scale fluctuating velocity $u_l'(\boldsymbol{x},t)=G_{\mathcal{T}}\star u'(\boldsymbol{x},t)=G_{\mathcal{T}}\star[u(\boldsymbol{x},t)-U(z)]$, where $G_{\mathcal{T}}$ is a low-pass filter kernel at scale $\mathcal{T}$ (discussion to follow). Large-scale content embodied within $u_l'(\boldsymbol{x},t)$ modulates surface fluxes [27,31], with visualization of power spectral density over elevation and wavelength (spectrogram) confirming that the energetic content associated with VLSMs resides at a distinct "outer peak." Figure 1(a), derived from the neutral large-eddy simulation (LES) case outlined within Ref. [32], shows a spectrogram of streamwise velocity fluctuations. The flow depth (dashed line) is the demarcating scale between attached eddies and LSMs, which is consistent with the notion of wall-attached eddies being regulated in extent by z [12]. Figure 1(b) is the standard deviation of the large-scale signature, derived via Parseval's theorem (discussion to follow); Fig. 1(b) shows correlation in magnitude with the spectrogram, marking the signature of LSMs within the lowest 20% of the domain. Since LSMs are dynamically relevant, additional generality is needed. Herein, we argue that a "large-scale" velocity, u_l', can be readily incorporated, which guides reposing of the problem in dimensional form with five variables, u_τ, $\overline{w'\theta'}$, g/Θ_0, z, and u_l', yielding $\Pi_1=\phi_{m,l}(\Pi_2,\Pi_3)$ where Π_1 is again the dimensionless dependent variable of interest (mean vertical gradient), $\Pi_2=\zeta$, and

$$\Pi_3=\alpha(\boldsymbol{x},t)=\frac{u_l'(\boldsymbol{x},t)}{u_\tau}=\frac{u_l(\boldsymbol{x},t)-U(z)}{u_\tau} \tag{2}$$

is a new dimensionless parameter that accounts for the loading and unloading of surface layer flux-gradient relations imposed by the passage of LSMs and VLSM aloft. Thus, dimensional analysis predicts:

$$\frac{\kappa z}{u_\tau}\frac{\partial u_l(\boldsymbol{x},t)}{\partial z}=\phi_{m,l}[\zeta,\alpha(\boldsymbol{x},t)] \tag{3}$$

for the dimensionless large-scale mean velocity gradient. While one could formulate the new similarity framework in terms of the large-scale (not fluctuating) velocity $u_l(\boldsymbol{x},t) = G_{\mathcal{T}} \star u(\boldsymbol{x},t)$, u_l' is a more convenient choice since it allows us to define $\alpha(\boldsymbol{x},t) = 0$ as a case free from LSM modulation, i.e., when $u_l(\boldsymbol{x},t) = U(z)$, $\alpha(\boldsymbol{x},t) = 0$, and $\phi_{m,l}(\zeta,0) = \phi_m(\zeta)$, allowing recovery of classical MOST. If the new dimensional analysis is correct, the deviations of $\phi_{m,l}(\zeta,\alpha)$ from $\phi_m(\zeta)$ predicted by MOST should be a function of α [9], i.e.,

$$\frac{\phi_{m,l}[\zeta,\alpha(\boldsymbol{x},t)] - \phi_m(\zeta)}{\phi_m(\zeta)} = f[\alpha(\boldsymbol{x},t)]. \tag{4}$$

In order to comprehensively demonstrate the influence of LSMs in modulation of near-wall fluxes, we have used data from the advection horizontal array turbulence study (AHATS) field campaign [32]. The time-series measurements of streamwise velocity are low-pass filtered at timescale, $\mathcal{T}$, where $\mathcal{T}U(z)/\delta = 1$, which is equivalent (in frequency) to demarcation at $\lambda_x/\delta = 1$ [e.g., Fig. 1(a)]. We assumed a boundary layer depth of $\delta = 1000$ m; results were not significantly sensitive to choice of δ [32]. This yields a time-dependent flow field wherein only the large-scale motions (LSM) are preserved: $u_l(\boldsymbol{x},t) = G_{\mathcal{T}} \star u(\boldsymbol{x},t)$. Figure 1(e) shows the evolution of $u_l(\boldsymbol{x},t)$ and α, where quantitative values are denoted on the left and right ordinates, respectively. Figure 1(f) shows the ensemble mean of the correlation coefficients between $u_l(\boldsymbol{x},t)$ and $\alpha(\boldsymbol{x},t)$ (red markers and gray bands denote average and standard deviation, respectively). This correlation is physically interpreted as a systematic loading and unloading, or modulation, via the passage of LSMs aloft; a graphical illustration in terms of the streamwise velocity and the accompanying gradient is presented in Figs. 1(g) and 1(h), respectively.

Figure 1(c) shows data points from the AHATS campaign, revealing a pronounced linear scaling between the left- and right-hand sides of Eq. (4), enabling:

$$\begin{aligned} f[\alpha(\boldsymbol{x},t)] &= \mathcal{C}_0 + \mathcal{C}_1\alpha(\boldsymbol{x},t) \text{ and} \\ \phi_{m,l}[\zeta,\alpha(\boldsymbol{x},t)] &= \phi_m(\zeta)\{1 + f[\alpha(\boldsymbol{x},t)]\}. \end{aligned} \tag{5}$$

In the absence of large-scale modulation, $\alpha(\boldsymbol{x},t) = 0$, and $\phi_{m,l}[\zeta,\alpha(\boldsymbol{x},t) = 0] \to \phi_m(\zeta)$, enforcing the condition $\mathcal{C}_0 = 0$. An empirical fit of Eq. (5) to the AHATS data yields $\mathcal{C}_1 = 0.10$. This result demonstrates that $\alpha(\boldsymbol{x},t)$ captures large-scale modulation [27,30], which also occurs for unstable stratification [31]; a recent article has revealed an ostensible LSM structural invariance for unstable conditions [48], indicating that the underlying conceptual approach is valid across ζ. For cases where loading or unloading is negligible [small $|\alpha(\boldsymbol{x},t)|$], the vertical gradient tends towards the classical MOST empirical curves [1,49,50].

Figure 1(d) presents results from the AHATS data of generalized velocity gradient $\phi_{m,l}$ [Eq. (5)] against stability parameter ζ (abscissa), grouped based upon the value of $\alpha(\boldsymbol{x},t)$. The data points are color coded, for perspective, and there is a distinct positive and negative vertical shift for $\alpha(\boldsymbol{x},t) > 0$ and $\alpha(\boldsymbol{x},t) < 0$, respectively, consistent with the aforementioned notion of additional loading and unloading of the velocity gradient with the passage of LSMs aloft. The functional form of the empirical $\phi_{m,l}(\zeta,\alpha)$ curves can be established by noting that Eq. (5) implies $\phi_{m,l}(\zeta,\alpha) = \phi_m(\zeta)[1 + \mathcal{C}_1\alpha(\boldsymbol{x},t)]$. Using the Businger-Dyer [49] empirical curves we therefore have

$$\phi_{m,l}(\zeta,\alpha) = (1 - 16\zeta)^{-1/4}[1 + \mathcal{C}_1\alpha]. \tag{6}$$

In addition, the O'KEYPS closure—an interpolation formula that captures the observed scaling of ϕ_m under stable, neutral, and unstable conditions—can be generalized for large-scale modulation [32], yielding

$$\phi_{m,l}^4(\zeta,\alpha) - \gamma\zeta\phi_{m,l}^3(\zeta,\alpha) - (1 + \mathcal{C}_1\alpha)^4 = 0. \tag{7}$$

Empirical curves corresponding to Eqs. (6) and (7) are overlaid on Fig. 1(d). In this approach, $\alpha(\boldsymbol{x},t)$ is varied *a priori*, but the results agree closely with the field data. This result demonstrates that generalized application of MOST is tractable, with modulation by LSMs central in explaining the data spread that might otherwise be attributed to scatter.

Prognostic closure.—In this section, we present a prognostic closure for the large-scale velocity profile as a function of the MOST stability parameter ζ and the modulation parameter $\alpha(\boldsymbol{x},t)$. Figure 2(a) shows a time-height contour [51] of streamwise velocity from neutrally stratified LES, with thick black lines superimposed to highlight LSM inclination. Figure 3(a) shows vertical profiles of conditionally sampled velocity, $\langle \tilde{u}/u_\tau | \alpha(\boldsymbol{x},t) \rangle_{xyt}$ (where $\langle \cdots \rangle_a$ denotes averaging over dimension a), with the sampling thresholds indicated on the panel. The signature of loading and unloading of the surface-layer gradient [Figs. 1(g) and 1(h)] is abundantly clear in Fig. 3(a). It is appropriate to pose these results in the context of contemporary findings on uniform momentum zones (UMZ) [52], which encompass both high- and low-momentum regions. These structures are spatially bound by interfacial layers of elevated gradients [53]. We have used the fuzzy clustering method [54] to identify UMZs in the LES data [light black lines in Fig. 2(a)]. At three arbitrary times the vertical profiles of streamwise velocity are shown on Fig. 2(b), which confirm the "staircaselike" velocity distribution that is the signature of UMZs (for example, $tu_\tau\delta^{-1} = 0.5$ and $z/\delta \approx 0.18$ and 0.45). Non-MOST values of the near-wall gradient can be explained via excursions in the large-scale velocity—consistent with related findings on the dynamics of UMZs.

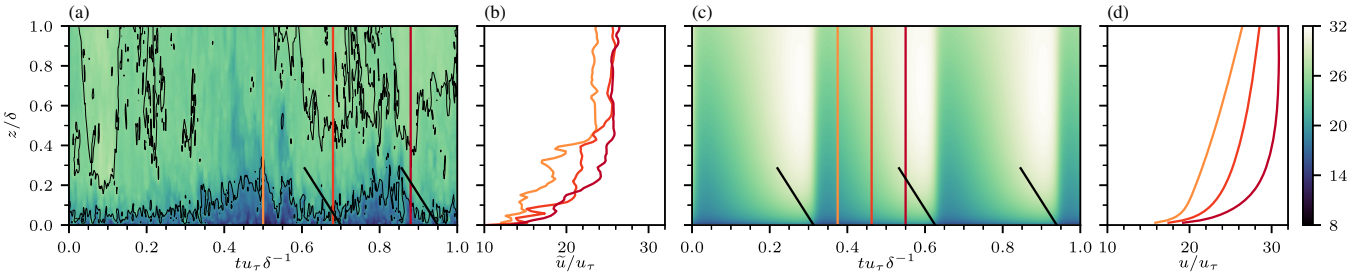

FIG. 2. Contours of dimensionless streamwise velocity ($\tilde{u}/u_\tau$) as a function of dimensionless time $tu_\tau\delta^{-1}$ and height z/δ from (a) neutrally stratified LES and (c) PDE solution. Heavy black lines indicate inclination angles, $\theta = \tan^{-1}[-U_0 u_\tau^{-1}\tan(\gamma)]$, where $\gamma = 17°$ is the spatial inclination angle for LSMs and U_0 is the advection velocity; thin black lines in (a) denote interfaces between uniform momentum zones (UMZ). A dimensionless frequency of $\hat{\omega} = (U_0\delta)(u_\tau\lambda_x)^{-1}$ is used when computing the PDE solution in (c), with an LSM wavelength of $\lambda_x = \pi\delta$. Vertical lines on (a) and (c) denote sampling times, with the corresponding profiles superimposed on (b) and (d), respectively; the LES profiles reveal the "staircaselike" pattern associated with UMZs [52,53].

Given the reported linear scaling between $\alpha(\boldsymbol{x}, t)$ [Eq. (2)] and the nondimensional gradient [Eq. (5)], one may develop a prognostic model for *a priori* prediction of the large-scale content, $u_l(z, t)$. By equating Eqs. (3) and (5) we have the following:

$$\frac{\kappa z}{u_\tau}\frac{\partial u_l(\boldsymbol{x}, t)}{\partial z} = \phi_m(\zeta)[\mathcal{C}_0 + \mathcal{C}_1\alpha(\boldsymbol{x}, t)]. \tag{8}$$

For a horizontally homogeneous atmospheric boundary layer under neutral or unstable stratification ($\zeta \leq 0$), a series of modest algebraic developments yields this:

$$\frac{\partial u_l(z, t)}{\partial z} = \frac{u_\tau}{\kappa z}\phi_m(\zeta)[1 + \mathcal{C}_1\alpha(z, t)]. \tag{9}$$

Equation (9) can be integrated, yielding [32]

$$u_l(z, t) = \frac{u_\tau}{\kappa}\left[\ln\frac{z}{z_0} - \Psi_m(\zeta)\right] + \frac{\mathcal{C}_1 u_\tau}{\kappa}\int z^{-1}\phi_m(\zeta)\alpha(z, t)dz. \tag{10}$$

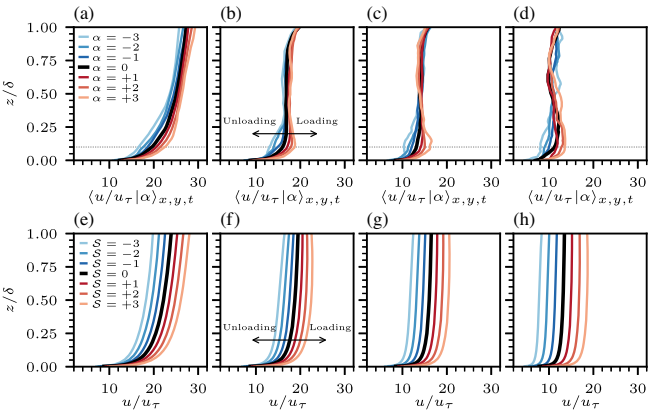

FIG. 3. (a)–(d) Conditionally sampled mean velocity profiles, i.e., $\langle\tilde{u}/u_\tau|\alpha(\boldsymbol{x}, t)\rangle_{xyt}$ from neutrally stratified LES. (e)–(h) Velocity profiles U/u_τ from PDE solution for a range of $\mathcal{S}$ values. (a),(e) $-\delta/L = 0$; (b),(f) $-\delta/L = 3.16$; (c),(g) $-\delta/L = 17.7$; (d),(h) $-\delta/L = 80.3$

The first term on the right hand side of (10) is the "base state" given by the classical MO similarity where z_0 is an aerodynamic roughness length, and $\Psi_m(\zeta) = \int_{z_0/L}^{\zeta}[1 - \phi_m(\xi)]d\xi$ is the integrated stability correction function. The second term on the rhs of Eq. (10) encapsulates the modulating influence of LSMs. In order to proceed, the wall-normal and temporal dependence of $\alpha(z, t)$ must be specified. Because the signature of LSMs appear as a distinct "outer peak" in $E_{\langle u'(\boldsymbol{x},t)^2\rangle_t}(\lambda_x, z)$ in the range, $10^0 \lesssim \lambda_x/\delta \lesssim L_x/\delta$ and $10^{-1} \lesssim z/\delta \lesssim 3\times10^{-1}$, where L_x is the integral length associated with VLSMs [22], Parseval's theorem can be used to recover the general form for $\alpha(z)$:

$$[\hat{\alpha}(z)]^2 = u_\tau^{-2}\int_\delta^{L_x} E_{\langle u'(\boldsymbol{x},t)^2\rangle_t}(\lambda_x, z)d\lambda_x. \tag{11}$$

Figure 1(a) shows a spectrogram of $E_{\langle u'(\boldsymbol{x},t)^2\rangle_t}(\lambda_x, z)$, for the neutral LES reviewed in Ref. [32]. For reference, a dashed black line at $\lambda_x/\delta = 10°$ has been superimposed on Fig. 1(a), highlighting the separation wavelength between attached eddies and VLSMs; as per Eq. (11), $|\alpha(z, t)|$ is recovered via Parseval's theorem, which is shown on Figure 1(b). (Profiles of α for other δ/L values cases can be found in [32]). The panel shows that $|\alpha(z, t)|$ is largest at $z/\delta \approx 10^{-1}$, which coincides with the center of the outer peak.

Informed by these insights from the spectrograms, we introduce the ansatz

$$\alpha(z, t; \delta/L) = \mathcal{S}(\omega t)\sum_n a_n(\delta/L)g_n(z/\delta), \tag{12}$$

where α is projected onto polynomial basis functions $g_n(z/\delta) = (z/\delta)^n$ with coefficients $a_n(\delta/L)$. Time dependence is introduced through a sawtooth function $\mathcal{S}(\omega t)$, which is helpful for capturing the loading and unloading of the near-wall gradient due to the passage of large-scale motions aloft [30,51,55]. Here $\omega = U_0/\lambda_x^{op}$ is the

characteristic frequency of LSMs, where U_0 is an advective velocity scale, and λ_x^{op} is the streamwise wavelength of LSMs corresponding to the outer peak in spectrograms [Fig. 1(a)], which varies with δ/L [31]. While a projection onto sixth-order polynomials yields $\alpha(z)$ profiles in good agreement with those calculated from LES, we find that including only the a_0 term (i.e., constant α with height) yields velocity profiles in good agreement with the full sixth-order polynomial [32]. Upon substituting (12) into (10) and carrying out the integration, we arrive at

$$u_l(z,t) = \frac{u_\tau}{\kappa}\left[\ln\frac{z}{z_0} - \Psi_m(\zeta)\right][1 + \mathcal{C}_1 a_0(\delta/L)\mathcal{S}(\omega t)], \quad (13)$$

which holds for $\zeta \leq 0$; for neutral conditions ($\zeta = 0$), (13) reduces to

$$u_l(z,t) = \frac{u_\tau}{\kappa}\ln\frac{z}{z_0}[1 + \mathcal{C}_1 a_0(0)\mathcal{S}(\omega t)]. \quad (14)$$

Figure 2(c) shows time-height contour predictions from Eq. (13). The contours lack the extensive range of dynamical scales evident in Fig. 2(a), but possess the salient features of the passage of LSMs. Given the lack of physical scales present, UMZs and associated interfacial shear layers are not predicted by the PDE solution, which is apparent from consultation of Figs. 2(c) and 2(d); Fig. 2(d) does, however, provide clear illustration of the aforementioned surface-layer loading and unloading, which is responsible for deviation from ensemble-mean MOST predictions [Figs. 1(g) and 1(h)]. LES flow fields were conditionally sampled based on the value of $\alpha(\boldsymbol{x}, t)$ for simulations spanning several values of $-\delta/L$, with results displayed in Figs. 3(a)–3(d). Modulated velocity profiles from the prognostic model [Eq. (13)] are displayed in Figs. 3(e)–3(h) for several values of the sawtooth function $\mathcal{S}$. The profiles from the prognostic model demonstrate good agreement with LES results, and indicate the existence of a family of velocity profiles (for a given stability ζ) increasing with $\alpha(\boldsymbol{x}, t)$. Thus, it is clear that the modeling approach, generalized for LSMs, captures realistic features of the resultant velocity profile.

Conclusion.—In an ensemble-mean sense, Monin-Obukhov similarity theory predicts nondimensionalized vertical gradients of quantities of interest (momentum, heat, water vapor, etc.). Numerical weather prediction requires a closure for wall fluxes, which has seen MOST used in a time-local sense, precluding agreement between the instantaneous and ensemble-mean gradients; this is commonly attributed to "scatter," when inclusion of salient independent parameters would yield additional dimensionless groups that collapse the data. One candidate parameter is a large-scale velocity associated with LSMs meandering within the flow. Support for this choice is derived from findings over the last decade that LSMs distinctly modulate the amplitude and frequency of inner-layer processes [27,28,30,31]. Data from a comprehensive field campaign [32] were used to demonstrate efficacy of large-scale velocity as an additional independent parameter, and to develop a prognostic model for the effect of large-scale modulation upon the near-surface gradient. A generalized model for the near-wall gradient and a prognostic model for the large-scale velocity streamwise velocity were found to agree closely with field data and results from large-eddy simulation.

This work was supported by the National Science Foundation, Grant No. AGS-1500224 (W. A.).

*salesky@ou.edu

[1] J. A. Businger, J. C. Wyngaard, Y. Izumi, and E. F. Bradley, J. Atmos. Sci. **28**, 181 (1971).
[2] J. C. Kaimal, J. Wyngaard, Y. Izumi, and O. Coté, Q. J. R. Meteorol. Soc. **98**, 563 (1972).
[3] S. Pope, *Turbulent Flows* (Cambridge University Press, Cambridge, 2000).
[4] J. W. Deardorff, Mon. Weather Rev. **100**, 93 (1972).
[5] J.-F. Louis, Bound.-Lay. Meteorol. **17**, 187 (1979).
[6] H. A. Panofsky, H. Tennekes, D. H. Lenschow, and J. Wyngaard, Bound.-Lay. Meteorol. **11**, 355 (1977).
[7] S. Khanna and J. G. Brasseur, J. Fluid Mech. **345**, 251 (1997).
[8] C. Johansson, A.-S. Smedman, U. Högström, J. G. Brasseur, and S. Khanna, J. Atmos. Sci. **58**, 1549 (2001).
[9] S. T. Salesky and M. Chamecki, J. Atmos. Sci. **69**, 3700 (2012).
[10] Q. Li, P. Gentine, J. P. Mellado, and K. A. McColl, J. Atmos. Sci. **75**, 3403 (2018).
[11] J. Lumley and H. Panofsky, *The Structure of Atmospheric Turbulence* (John Wiley and Sons, New York, 1964).
[12] A. Townsend, Math. Proc. Cambridge Philos. Soc. **47**, 375 (1951).
[13] L. S. Kovasznay, V. Kibens, and R. F. Blackwelder, J. Fluid Mech. **41**, 283 (1970).
[14] G. L. Brown and A. S. Thomas, Phys. Fluids **20**, S243 (1977).
[15] C. E. Wark and H. Nagib, J. Fluid Mech. **230**, 183 (1991).
[16] R. J. Adrian, C. D. Meinhart, and C. D. Tomkins, J. Fluid Mech. **422**, 1 (2000).
[17] B. Ganapathisubramani, E. K. Longmire, and I. Marusic, J. Fluid Mech. **478**, 35 (2003).
[18] R. J. Adrian, Phys. Fluids **19**, 041301 (2007).
[19] K. Kim and R. Adrian, Phys. Fluids **11**, 417 (1999).
[20] M. Guala, S. Hommema, and R. Adrian, J. Fluid Mech. **554**, 521 (2006).
[21] B. Balakumar and R. Adrian, Phil. Trans. R. Soc. A **365**, 665 (2007).
[22] N. Hutchins and I. Marusic, J. Fluid Mech. **579**, 1 (2007).
[23] I. Marusic and N. Hutchins, Flow Turbul. Combust. **81**, 115 (2008).
[24] W. Willmarth and S. Lu, J. Fluid Mech. **55**, 65 (1972).
[25] J. M. Wallace, Annu. Rev. Fluid Mech. **48**, 131 (2016).
[26] R. Mathis, N. Hutchins, and I. Marusic, J. Fluid Mech. **628**, 311 (2009).

[27] I. Marusic, R. Mathis, and N. Hutchins, Science **329**, 193 (2010).
[28] B. Ganapathisubramani, N. Hutchins, J. Monty, D. Chung, and I. Marusic, J. Fluid Mech. **712**, 61 (2012).
[29] W. Baars, K. Talluru, N. Hutchins, and I. Marusic, Exp. Fluids **56**, 188 (2015).
[30] W. Anderson, J. Fluid Mech. **789**, 567 (2016).
[31] S. T. Salesky and W. Anderson, J. Fluid Mech. **856**, 135 (2018).
[32] See the Supplemental Material at http://link.aps.org/supplemental/10.1103/PhysRevLett.125.124501, which includes additional information on field campaign data, numerical simulations, and full derivations of the prognostic model for modulated mean velocity profile, a generalized version of the O'KEYPS equation, and Refs. [33–46].
[33] J. Albertson and M. Parlange, Water Resour. Res. **35**, 2121 (1999).
[34] E. Bou-Zeid, C. Meneveau, and M. Parlange, Phys. Fluids **17**, 025105 (2005).
[35] J. Businger, Bound.-Lay. Meteorol. **42**, 145 (1988).
[36] V. Canuto and Y. Cheng, Phys. Fluids **9**, 1368 (1997).
[37] G. G. Katul, A. G. Konings, and A. Porporato, Phys. Rev. Lett. **107**, 268502 (2011).
[38] J. Kleissl, V. Kumar, C. Meneveau, and M. B. Parlange, Water Resour. Res. **42** W06D10, (2006).
[39] C. Meneveau and I. Marusic, J. Fluid Mech. **719**, R1 (2013).
[40] C.-H. Moeng and P. P. Sullivan, J. Atmos. Sci. **51**, 999 (1994).
[41] S. Orszag, J. Atmos. Sci. **27**, 890 (1970).
[42] E. Plate, *AEC Critical Review Series* (U.S. Atomic Energy Commission, Springfield, VA, 1971).
[43] F. Porté-Agel, Bound.-Lay. Meteorol. **112**, 81 (2004).
[44] S. T. Salesky, M. Chamecki, and E. Bou-Zeid, Bound.-Lay. Meteorol. **163**, 41 (2017).
[45] R. J. Stevens, M. Wilczek, and C. Meneveau, J. Fluid Mech. **757**, 888 (2014).
[46] R. Stoll and F. Porté-Agel, Water Resour. Res. **42**, W01409 (2006).
[47] S. T. Salesky, M. Chamecki, and N. L. Dias, Bound.-Lay. Meteorol. **144**, 113 (2012).
[48] S. T. Salesky and W. Anderson, J. Fluid Mech. **884**, R5 (2019).
[49] A. Dyer, Bound.-Lay. Meteorol. **7**, 363 (1974).
[50] U. Högström, Bound.-Lay. Meteorol. **42**, 55 (1988).
[51] W. Anderson, Q. Li, and E. Bou-Zeid, J. Turbul. **16**, 809 (2015).
[52] C. Meinhart and R. Adrian, Phys. Fluids **7**, 694 (1995).
[53] M. Heisel, C. de Silva, N. Hutchins, I. Marusic, and M. Guala, J. Fluid Mech. **887**, R1 (2020).
[54] D. Fan, J. Xu, M. Yao, and J.-P. Hickey, J. Fluid Mech. **872**, 198 (2019).
[55] P. Sullivan, J. Weil, E. Patton, H. Jonker, and D. Mironov, J. Atmos. Sci. **73**, 1815 (2016).